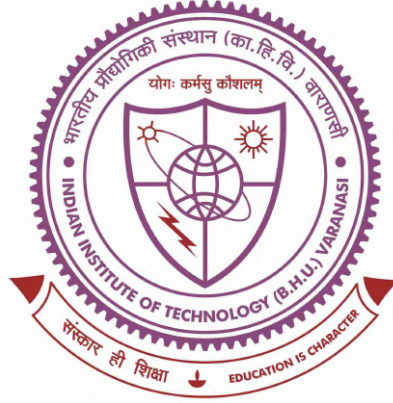


**Role of atomic ordering in tuning physical properties of  
 $K_{0.5}Na_{0.5}NbO_3$ -based smart materials**



**Thesis submitted in partial fulfillment  
for the Award of  
DOCTOR OF PHILOSOPHY  
in  
PHYSICS**

*by*  
**ANUVRAT TRIPATHI**

*Under the supervision of*  
**Dr. Saurabh Tripathi**

**DEPARTMENT OF PHYSICS  
INDIAN INSTITUTE OF TECHNOLOGY  
BANARAS HINDU UNIVERSITY  
VARANASI - 221 005**

**ROLL NUMBER  
19171006**

**YEAR OF SUBMISSION  
2025**

*I would dedicate this thesis to my loving parents, my sisters, and my amazing family-like friends, whose support and motivation kept me going through the tough times.*

## Certificate

It is certified that the work contained in the thesis titled “**Role of atomic ordering in tuning physical properties of  $K_{0.5}Na_{0.5}NbO_3$ -based smart materials**” by **Mr. Anuvrat Tripathi**, Roll Number **19171006**, has been carried out under my supervision and that this work has not been submitted elsewhere for a degree.

It is further certified that the student has fulfilled all the requirements of the Comprehensive Examination, Candidacy, and SOTA for the award of Ph.D. Degree in Physics.

Date of Submission: 25<sup>th</sup> June, 2025

Signature:



Supervisor

Dr. Saurabh Tripathi

(Associate Professor)

Department of Physics

Indian Institute of Technology (BHU),

Varanasi-221005 (U.P.), India

Associate Professor

Department of Physics

Indian Institute of Technology,

(Banaras Hindu University)


Varanasi-221005

## Declaration

I, **Anuvrat Tripathi**, certify that the work embodied in this thesis is my own bona-fide work and carried out by me under the supervision of **Dr. Saurabh Tripathi** from July 2019 to June 2025 at the **Department of Physics, Indian Institute of Technology (BHU), Varanasi**. The matter embodied in this thesis has not been submitted for the award of any other degree/diploma. I declare that I have faithfully acknowledged and given credits to the research workers whenever and wherever their works have been cited in my work in this thesis. I further declare that I have not willfully copied any others' work, paragraphs, text, data, results, etc., reported in journals, books, magazines, reports, dissertations, theses, etc., or available at websites and have not included them in this thesis and have not cited as my own work.

Date: 25<sup>th</sup> June, 2025


Place: IIT (BHU), Varanasi


  
Signature of the Student

(Anuvrat Tripathi)

## Certificate by the Supervisor

It is certified that the above statement made by the student is correct to the best of my knowledge.

Signature:   
Supervisor  
(Dr. Saurabh Tripathi)  
Associate Professor  
Department of Physics  
Indian Institute of Technology  
(Banaras Hindu University)  
Varanasi-221005

  
Signature of the Head of the Department  
HEAD / विभागाध्यक्ष  
भौतिकी विभाग / Deptt. of Physics  
भा.प्रौ.सं. / (का.हि.वि.) / IIT (BHU)  
वाराणसी / Varanasi-221005

## Copyright Transfer Certificate

**Title of the Thesis :** Role of atomic ordering in tuning physical properties of  $K_{0.5}Na_{0.5}NbO_3$ -based smart materials


**Name of the Student :** Anuvrat Tripathi

### Copyright Transfer

The undersigned hereby assigns to the Indian Institute of Technology (Banaras Hindu University) Varanasi all rights under copyright that may exist in and for the above thesis submitted for the award of the **Doctor of Philosophy in Physics**.

Date: 25<sup>th</sup> June, 2025

Place: IIT (BHU), Varanasi

  
Signature of the Student

(Anuvrat Tripathi)

**Note:** However, the author may reproduce or authorize others to reproduce material extracted verbatim from the thesis or derivative of the thesis for author's personal use provided that the source and the Institute's copyright notice are indicated.

## Acknowledgements

*I bow down with deep gratitude to Almighty Mahadev for everything, whose divine blessings have guided me at every step of this journey.*

First, I would like to express my sincere gratitude to my supervisor, **Dr. Saurabh Tripathi**, for his unwavering guidance, insightful mentorship, and continuous encouragement over the past five years. His constant support has been instrumental in shaping my research and academic growth.

I am profoundly thankful to my beloved parents, **Mr. Uma Shanker Tripathi and Mrs. Nirmala Tripathi**, and my sisters **Nishi Trivedi, Neha Trivedi, Krati Mishra, Kamayani Trivedi, and Katyayani Trivedi** for their constant support and encouragement. I am equally grateful to my family-like companions **Neha, Shweta, and Pawan**, for their continuous emotional support and constant motivation throughout this academic journey.

I extend my heartfelt gratitude to my Research Progress Evaluation Committee (RPEC) members, **Prof. Sandip Chatterjee** and **Prof. Akhilesh Kumar Singh**, for their valuable suggestions, constructive feedback, and continuous encouragement during the course of my research.

I am thankful to the Head of the Department, all the faculty members, and the non-teaching staff of the Department of Physics, IIT (BHU), for providing a conducive academic environment and their support throughout my Ph.D. journey.

I would like to express my gratitude to our collaborators **Prof. Valeri Petkov** (Central Michigan University), **Dr. Abhishek Pandey** (University of Witwatersrand), **Dr. Rudolph Erasmus** (University of Witwatersrand), **Dr. Sanjit Ghose** (Brookhaven National Laboratory), **Prof. Jose Antonio Alonso** (Instituto de Ciencia de Materiales de Madrid, C.S.I.C.), for their help in carrying out different measurements as per our requirements and also for

their various comments and suggestions. I would also like to express my gratitude to **Mr. Gaurav Rudra Malik** for his technical discussions.

I would also like to extend my gratitude to my batchmates and friends **Pawan, Kaushtubh, Harsh, Sachin, Subham, Ashish, Santosh, Shweta, Samiksha, Neha, Akanksha, Kartika, and Manisha.**

Finally, I would like to extend my gratitude to my senior (**Dr. Digvijay Nath Dubey**), fellow scholars (**Mr. Prosun Mondal**) and lab mates (**Mr. Harsh Kumar, Ms. Tanu Swami, Mr. Ajay Singh, Mr. Sanjeev Kumar, and Mr. Kartikey Chaturvedi.**)

**Anuvrat Tripathi**

# List of figures

1.1	The hysteresis loop illustrates the relationship between polarization and the electric field (P-E) for a typical ferroelectric material. Here, $P_r$ and $E_c$ correspond to remnant polarization and the coercive field, respectively. . . . .	3
1.2	Representation of direct and converse piezoelectric effect [1]. . . . .	5
1.3	The unit cell of an ideal cubic perovskite ( $ABO_3$ ) structure. . . . .	7
1.4	The representation of different points <i>viz.</i> , $\Gamma$ ( $q = 0,0,0$ ), $R$ ( $q = \frac{1}{2}, \frac{1}{2}, \frac{1}{2}$ ), $M$ ( $q = \frac{1}{2}, \frac{1}{2}, 0$ ), and $X$ ( $q = \frac{1}{2}, 0, 0$ ) in the Brillouin zone of the cubic lattice [2].	11
1.5	Representation of polymorphic phase boundary (PPB) and morphotropic phase boundary (MPB) existing between two ferroelectric phases <i>viz.</i> , $F_1$ and $F_2$ . . . . .	14
1.6	Morphotropic phase boundary in $Pb(Zr,Ti)O_3$ (PZT) ceramics [3]. . . . .	15
1.7	Schematic representation of polar directions in monoclinic $M_A$ , $M_B$ , and $M_C$ phases [4]. . . . .	15
1.8	The figure represents the frequency-dependent real part of the dielectric constant of relaxor ferroelectric <i>viz.</i> , $Pb(Mg, Nb)O_3$ [5]. . . . .	18
1.9	Slim P-E loop observed for a relaxor ferroelectrics [6, 7]. Here, $P_R$ and $E_C$ correspond to remnant polarization and coercive field, respectively. . . . .	18
1.10	Schematic representation of polar nanoregions in the non-polar (cubic) matrix. . . . .	19

1.11 (A) Temperature-dependent evolution of dielectric constant for KNbO <sub>3</sub> single crystal [8, 9], and (B) Temperature-dependent evolution of dielectric constant and loss for KNbO <sub>3</sub> ceramics [9, 10]. . . . .	25
1.12 Temperature-dependent phase evolution of NaNbO <sub>3</sub> reported by Mishra <i>et al.</i> [11]. . . . .	26
1.13 Evolution of dielectric constant as a function of the temperature of BaTiO <sub>3</sub> [12]. . . . .	29
1.14 Temperature-dependent evolution of dielectric constant of SrTiO <sub>3</sub> . Here, T <sub>st</sub> represents the transition temperature from cubic (Space Group: $Pm\bar{3}m$ ) to tetragonal (Space Group: $I4/mcm$ ) phase [13]. . . . .	30
1.15 Phase diagram of (Ba,Sr)TiO <sub>3</sub> [14]. . . . .	31
1.16 Morphotropic Relaxor Boundary in KBT <sub>x</sub> system [15]. . . . .	31
2.1 Instruments used in the sample synthesis <i>via</i> solid-state reaction method. . . . .	37
2.2 Schematic representation of X-ray diffraction in a crystal. . . . .	39
2.3 (a) Bench-top XRD and (b) HR-XRD used for diffraction measurements. . . . .	40
2.4 X-ray vs Neutron scattering amplitudes. . . . .	40
2.5 BT-SEM used for microstructural analysis. . . . .	43
2.6 Keysight LCR meter used for dielectric measurements. . . . .	46
2.7 Different shapes of P-E loops. . . . .	48
2.8 Polarization <i>vs.</i> electric field (P-E) loop tracer by Radiant technologies. . . . .	48
2.9 Raman Instrument used for room temperature measurements. . . . .	51
3.1 X-ray diffraction peaks evolution of KNN <sub>x</sub> ( $x = 0.40, 0.50, \text{ and } 0.60$ ) ceramics with insets showing the evolution of the main perovskite peaks <i>viz.</i> , {200}, {220}, and {222} of KNN <sub>x</sub> ceramics. . . . .	60

3.2	Fitted profiles of {200} reflections of KNN <sub>x</sub> ceramics depicting FWHM difference ( $\Delta = \delta_{(200)/(002)} - \delta_{(020)}$ ) for (a) KNbO <sub>3</sub> , (b) $x = 0.40$ (KNN40), (c) $x = 0.50$ (KNN50), and (d) $x = 0.60$ (KNN60) ceramics. . . . .	61
3.3	Rietveld Analysis of KNN <sub>x</sub> ( $x = 0.40, 0.50, \text{ and } 0.60$ ) ceramics with insets showing the fits of {200}, {220}, and {222} peaks. The continuous black line represents the simulated patterns while the open red circles represents the observed pattern. The Bragg reflections are represented by vertical black bars, and the continuous blue line at the bottom represents the difference between observed and simulated patterns. . . . .	64
3.4	Evolution of lattice parameters ( $a, b, \text{ and } c$ ) with left inset showing the anomaly observed in $\beta$ parameter and right inset showing the volume of LRO structures of KNN <sub>x</sub> ( $x = 0.40, 0.50, \text{ and } 0.60$ ) ceramics. . . . .	66
3.5	The top figure represents the Raman spectra of KNN <sub>x</sub> ceramics and the bottom figure represents the Raman intensity of $\nu_1$ and $\nu_5$ peaks. . . . .	67
3.6	Observed PDF profile of KNN <sub>x</sub> ( $x = 0.40, 0.50, \text{ and } 0.60$ ) ceramics for $1.7 \leq r \leq 40$ . . . . .	68
3.7	Observed and fitted PDF profile of KNN <sub>x</sub> ( $x = 0.40, 0.50, \text{ and } 0.60$ ) ceramics for $r \leq 10 \text{ \AA}$ where the black pattern represents the observed data, yellow fit represents the monoclinic ( $Pm$ ) phase, and red fit represents the orthorhombic ( $Amm2$ ) phase. . . . .	69
3.8	Unit cell volume at long and short ranges for KNN <sub>x</sub> ( $x = 0.40, 0.50, \text{ and } 0.60$ ) ceramics. . . . .	70
3.9	Monoclinic angle $\beta$ at LRO and SRO of KNN <sub>x</sub> ( $x = 0.40, 0.50, \text{ and } 0.60$ ) ceramics with inset showing the difference in the monoclinic angle at LRO and SRO. . . . .	72

- 3.10 The separation parameter ( $\delta d$ ) plotted against the increasing potassium content ( $x$ ) for SRO and LRO with inset showing the difference of the separation ( $\delta d$ ) between SRO and LRO given as  $D=(\delta d_{\text{SRO}} - \delta d_{\text{LRO}})$  for KNN $_x$  ceramics. . . . . 73
- 3.11 The description of (a)  $\Gamma_4^-$  and (b)  $\Gamma_5^-$  phonon modes with OPD. The A-site atoms (purple) are at corner, B-site atom (green) at body center, and oxygen atoms (red) are at face center. The arrows represents the direction of atoms displacement. The figures were obtained from VESTA software [16]. . . . . 75
- 3.12 Mode amplitude of KNN $_x$  ( $x = 0.40, 0.50, \text{ and } 0.60$ ) ceramics at LRO and SRO with red color representing the LRO structures while green color representing SRO structures. . . . . 76
- 4.1 X-ray diffraction patterns of KBST $_x$  ceramics for  $0.00 \leq x \leq 0.20$  and the evolution of the main perovskite peaks *viz.*, {200}, {220}, and {222} as a function of composition. . . . . 84
- 4.2 The XRD profiles of KBST $_x$  ceramics at ambient conditions fitted using Rietveld analysis. Different models have been used for fitting *viz.*,  $Pm$  model for  $x = 0.00$ , ( $Pm + P4mm$ ) model for  $x = 0.05$  and  $0.10$ , and  $P4mm$  model for  $x = 0.15$ . Moreover, a cubic symmetry (Space Group:  $Pm\bar{3}m$ ) is used to fit the XRD profile for  $x = 0.20$  using the Le Bail method (Tripathi *et al.*, 2024) [7]. The open red circles represent the observed diffraction pattern, the black continuous line represents the calculated profile, and the blue line represents the difference between the observed and calculated patterns. . . . . 86

- 
- 4.3 The plot between real ( $\epsilon'$ ) and imaginary ( $\epsilon''$ ) part of dielectric constant of  $\text{KBST}_x$  ceramics. Here,  $T_{\text{M-T}}$ ,  $T_{\text{m}}$ , and  $T_{\text{C}}$  represent the temperature corresponding to the monoclinic to tetragonal phase transition, the temperature corresponding to the dielectric maxima, and the Curie temperature, respectively. . . . . 89
- 4.4 The plot between the inverse of the real part of the dielectric constant ( $\epsilon'$ ) and temperature ( $T$ ) for  $\text{KBST}_x$  ceramics. . . . . 90
- 4.5 Evolution of room temperature dielectric constant at 100 kHz for  $\text{KBST}_x$  ceramics. . . . . 90
- 4.6 Evolution of main perovskite peaks as a function of temperature ( $300 \text{ K} \leq T \leq 1000 \text{ K}$ ) of  $\text{KBST}_5$  ceramics. . . . . 92
- 4.7 Evolution of volume (at long ranges) of  $\text{KBST}_5$  ceramics as a function of temperature. . . . . 92
- 4.8 Evolution of the amplitude of ferroelectric phonon mode ( $\Gamma_4^-$ ) with compositions ( $x$ ). The top right inset represents the evolution of the overall amplitude of  $\Gamma_4^-$  phonon mode as a function of compositions ( $x$ ). Here, the amplitude of the  $\Gamma_4^-$  phonon mode has been calculated using the structural parameters obtained after Rietveld analysis of benchtop XRD data of  $\text{KBST}_x$  ceramics. . . . . 93
- 4.9 Evolution of the overall amplitude of  $\Gamma_4^-$  phonon mode of  $\text{KBST}_5$  as a function of temperature. Here, the amplitude of the  $\Gamma_4^-$  phonon mode has been calculated using the structural parameters obtained after Rietveld analysis of temperature-dependent SXRD data of  $\text{KBST}_5$  ceramics. . . . . 94

- 
- 4.10 The Raman spectra of  $\text{KBST}_x$  ceramics. The top left and top right inset represent the variation of wavenumber and intensity of  $\nu_2$  mode with compositions. The figures on the right represent the fitting of the prominent Raman peak ( $500\text{ cm}^{-1}$ - $700\text{ cm}^{-1}$ ) using the Lorentz function for  $\text{KBST}_x$  ceramics. . . . . 96
- 4.11 Evolution of temperature-dependent Raman spectra of  $\text{KBST}_5$  ceramics for  $77\text{ K} \leq T \leq 650\text{ K}$ . . . . . 100
- 4.12 Evolution of wavenumbers of modes around  $605\text{ cm}^{-1}$  and  $560\text{ cm}^{-1}$  as a function of temperature. . . . . 102
- 4.13 The experimental PDF profile of  $\text{KBST}_5$  ceramics at  $300\text{ K}$  ( $1.7\text{ \AA} \leq r \leq 10\text{ \AA}$ ). . . . . 103
- 4.14 Fitted PDF profiles of  $\text{KBST}_5$  ceramics as a function of temperature. The open circle, red line, and green line represent observed  $G(r)$ , fit using the tetragonal model (Space Group:  $P4mm$ ), and fit using the monoclinic model (Space Group:  $Pm$ ), respectively. Additionally, the orange and blue lines represent the difference lines between the calculated and observed  $G(r)$  pattern for  $P4mm$  and  $Pm$  models, respectively. . . . . 103
- 4.15 Evolution of volume of  $\text{KBST}_5$  ceramics at short ranges as a function of temperature. . . . . 105
- 4.16 Evolution of the amplitude of ferroelectric phonon mode ( $\Gamma_4^-$ ) at short ranges as a function of temperature for  $\text{KBST}_5$  ceramics. . . . . 105

- 5.1 (a) Temperature dependent neutron diffraction data of pure KBST20 ceramic for  $9 \text{ K} \leq T \leq 500 \text{ K}$ , (b), (c), (d) Temperature dependent evolution of  $\{200\}$ ,  $\{220\}$ , and  $\{222\}$  peaks respectively for  $9 \text{ K} \leq T \leq 500 \text{ K}$ , (e) Temperature dependent variation of volume for KBST20 ceramic where the symbol represents the experimental volume, solid curve represents the polynomial fit of experimental volume, and dashed curve represents nominal volume obtained from fitting of Debye-Grüneisen equation for  $380 \text{ K} \leq T \leq 500 \text{ K}$  [17, 18, 19] and (f). Variation of SVFS ( $\omega_s$ ) with temperature for  $9 \text{ K} \leq T \leq 380 \text{ K}$  where SVFS has been calculated using interpolated volume data. . . . . 113
- 5.2 Temperature-dependent Le Bail fits of KBST20 ceramics ( $9 \text{ K} \leq T \leq 500 \text{ K}$ ) with insets showing the fits of  $\{200\}$ ,  $\{220\}$ , and  $\{222\}$  peaks. The continuous black line represents the simulated patterns while the open red circles represents the observed pattern. The Bragg reflections are represented by vertical black bars, and the continuous blue line at the bottom represents the difference between observed and simulated patterns. 114
- 5.3 (a) Temperature-dependent dielectric permittivity ( $\epsilon'$ ) and loss ( $\tan\delta$ ) plot at various frequencies, (b) the zoomed-up view of the observed frequency dispersion ( $\Delta T \approx 27 \text{ K}$ ) with the same order of frequency as in 2(a), (c) the linear fitting of  $\ln(1/\epsilon' - 1/\epsilon'_{\max})$  vs.  $\ln(T - T_m)$  at 10 kHz for KBST20 ceramic, (d) Inverse of dielectric vs. temperature plot at 10 kHz, and (e) the Vogel-Fulcher law fitting for KBST20 ceramics. . . . . 117
- 5.4 Polarization vs Electric field response of KBST20 ceramics at 294 K and 223 K. . . . . 117

5.5	(a) Temperature-dependent Raman data for KBST20 ceramic, (b) zoomed-up view of polar peak ( $\nu_1 + \nu_5$ ) as a function of temperature, (c) the temperature-dependent intensity observed for prominent Raman modes ( $\nu_1$ , $\nu_2$ , and $\nu_5$ ). . . . .	120
5.6	Deconvolution of Raman peaks <i>viz.</i> , $\nu_5$ ( $\approx 245 - 265 \text{ cm}^{-1}$ ), $\nu_1$ and $\nu_2$ ( $\approx 500 - 700 \text{ cm}^{-1}$ ), for the temperature range $77 \text{ K} \leq T \leq 527 \text{ K}$ . . . . .	121
6.1	The X-ray diffraction plot of KBST $x$ ( $x = 0.90, 0.95$ , and $1.00$ ) ceramics with the evolution of main perovskite peaks <i>viz.</i> , $\{200\}$ , $\{220\}$ , and $\{222\}$ . . . . .	129
6.2	Rietveld fits of KBST $x$ ( $x = 0.90, 0.95$ , and $1.00$ ) ceramics with insets showing the fits of $\{200\}$ , $\{220\}$ , and $\{222\}$ peaks. The simulated patterns are depicted by the continuous black line, while the observed patterns are shown by the open red circles. The Bragg reflections are indicated by vertical black bars, and the difference between the observed and simulated patterns is represented by the continuous blue line at the bottom. . . . .	129
6.3	SEM picture of KBST90 ceramics along with histogram depicting the grain size distribution in KBST90 ceramics. . . . .	131
6.4	Electrical properties of KBST $x$ ceramics including (a)-(c) The temperature-dependent real ( $\epsilon'$ ) and imaginary ( $\epsilon''$ ) part of KBST $x$ ceramics, (d)-(f) the plot between the inverse of the real part of dielectric constant and temperature <i>i.e.</i> , $1/\epsilon'$ vs. $T$ for $x = 1.00, 0.95$ , and $0.90$ ceramics at $100 \text{ kHz}$ , (g) the frequency-dependent plot between real part of dielectric constant ( $\epsilon'$ ) with temperature for $x = 0.95$ and $0.90$ , (h) P-E loops for KBST $x$ ceramics, and (i)-(j) temperature-dependent P-E loops for KBST90 ceramics at $253 \text{ K}$ , $263 \text{ K}$ , and $300 \text{ K}$ . . . . .	132

- 6.5 (a)-(c) Temperature-dependent evolution of main perovskite peaks *viz.*, {200}, {220}, and {222} of KBST90 ceramics for  $100 \text{ K} \leq T \leq 500 \text{ K}$ , (d) Temperature-dependent evolution of volume for KBST90 ceramics. The symbols represent the experimental volume, whereas solid and dashed lines represent the polynomial fit of experimental volume and nominal volume ( $V_{nm}$ ), respectively. The inset shows the temperature-dependent evolution of Spontaneous Volume Ferroelectrostriction (SVFS) calculated using interpolated volume data. . . . . 135
- 6.6 The Raman spectra of KBST90 ceramics at 77 K, 300 K, and 527 K. Description of various modes has been mentioned on the top right of the figure [20, 21] also in Table 6.4. . . . . 137
- 6.7 The fitting of PDF profiles at various length scales *viz.*, (a) 1.7 Å- 10 Å, (b) 10 Å- 20 Å, (c) 15 Å- 25 Å, (d) 20 Å- 30 Å and, (e) 30 Å- 40 Å using *Pm* and *R3m* space groups for KBST90 ceramics. The black open circles denote observed PDF data, while orange and green lines correspond to *R3m* and *Pm* fit, respectively. The arrow represents the misfit observed by the *R3m* space group at  $r \leq 10 \text{ Å}$ . . . . . 139
- 6.8 Fitting of the temperature-dependent PDF profiles of KBST90 ceramics using monoclinic (*Pm*) and rhombohedral (*R3m*) space groups for  $1.7 \text{ Å} \leq r \leq 10 \text{ Å}$  at 100 K, 300 K, and 500 K. The open circles represent observed PDF data, while orange and green lines represent PDF fits for rhombohedral (*R3m*) and monoclinic (*Pm*) space groups. . . . . 140

6.9	Fitting of the temperature-dependent PDF profiles of KBST90 ceramics using rhombohedral ( $R3m$ ) space groups for $15 \text{ \AA} \leq r \leq 25 \text{ \AA}$ at 100 K, 300 K, and 500 K. The open circle represents the observed PDF data, while the red line represents the calculated PDF data, and the blue line represents the difference between observed and calculated data. . . . .	141
6.10	Temperature-dependent evolution of the amplitude of the ferroelectric phonon mode ( $\Gamma_4^-$ ) for $Pm$ ( $1.7 \text{ \AA} \leq r \leq 10 \text{ \AA}$ ), and $R3m$ ( $15 \text{ \AA} \leq r \leq 25 \text{ \AA}$ ) space group. . . . .	143
7.1	The evolution of $\{200\}$ , $\{220\}$ , and $\{222\}$ X-ray diffraction peak profiles for KBST $x$ ( $0.20 \leq x \leq 0.90$ ) ceramics. The black arrows indicate the additional broadening in the tails of the main perovskite peaks. The length of the arrows suggests the relative magnitude of the disorder in KBST $x$ ceramics. . . . .	151
7.2	(a) Deconvolution of main perovskite peaks <i>viz.</i> , $\{200\}$ , $\{220\}$ , and $\{222\}$ , and (b) Evolution of FWHM of the peak associated with additional broadening (green peak) as a function of composition ( $x$ ). . . . .	152
7.3	The top figures represent the evolution of Raman scattering data as a function of compositions at representative temperatures <i>i.e.</i> , (a) 77 K, (b) 300 K, (c) 377 K, and (d) 427 K. The bottom figures represent the temperature-dependent Raman scattering data for (e) KBST30, (f) KBST40, and (g) KBST50 ceramics. . . . .	153
7.4	Temperature-dependent evolution of Raman spectra of KBST $x$ ceramics for $0.20 \leq x \leq 0.90$ . The highlighted temperature (in orange color) represents Burns temperature ( $T_B$ ) for KBST $x$ ceramics. . . . .	155
7.5	Temperature-dependent observed $G(r)$ patterns of KBST40 ceramics.. . .	156

7.6	(a) Fitting of the PDF profiles of KBST40 ceramics at 8 K using $Pm$ , $R3m$ , and $Pm+R3m$ models. The inset of (a) shows the PDF profile fitting corresponding to B-O bonds. Evolution of the volume at short ranges for (b) $Pm$ (green symbols), (c) $R3m$ (blue symbols), (d) $Pm+R3m$ (orange symbols), at long ranges for (e) $Pm\bar{3}m$ (purple symbols) of KBST40 for $8\text{ K} \leq T \leq 495\text{ K}$ . The insets in (b)-(e) show negative thermal expansion (NTE) observed at very low temperatures at long/short ranges. Lastly, the evolution of ferroelectric mode ( $\Gamma_4^-$ ) as a function of temperature for (f) $Pm$ and (g) $R3m$ phase. . . . .	157
7.7	Temperature-dependent fitting of PDF profiles using $Pm$ , $R3m$ , and ( $Pm+R3m$ ) models for KBST40 ceramics. . . . .	158
7.8	Evolution of SVFS ( $\omega_S$ ) as function of temperature for different phases at short/long ranges. . . . .	159
7.9	Temperature-dependent dielectric of KBST40. The inset shows the plot between the inverse of the dielectric constant ( $1/\epsilon'$ ) and temperature (T). Here, $\Delta T_m$ is the difference between $T_B$ & $T_m$ and corresponds to disorder in the material [22]. . . . .	161
7.10	Evolution of main perovskite peaks <i>viz.</i> , {200}, {220}, and {222} as a function of temperature for KBST40 ceramics. . . . .	162
7.11	Evolution of linear CTE ( $\alpha_l$ ) values calculated at 100 K and 200 K for KBST20, KBST40, and KBST90 ceramics. . . . .	163
7.12	Morphotropic Relaxor Boundary in KBST $x$ ceramics. . . . .	164

# List of tables

1.1	Types of the Piezoelectric effect . . . . .	4
1.2	Different possible structures based on the tolerance factor (t) [23, 24]. . . . .	7
1.3	Different ferroelectric phases obtained after freezing of ferroelectric phonon mode $\Gamma_4^-$ giving rise to polarization along different directions. . . . .	9
1.4	Type of monoclinic phases with different polarization configuration and cation displacements. Here, R, O, and T represent rhombohedral, orthorhombic, and tetragonal phases, respectively. . . . .	16
1.5	Various phases exhibited by relaxor ferroelectrics as a function of temperature [25, 26]. . . . .	20
1.6	Temperature-dependent evolution of long-range crystal structure of $\text{NaNbO}_3$ reported by Jiang <i>et al.</i> [27]. . . . .	27
1.7	Phase evolution of $\text{KNN}_x$ ceramics. . . . .	28
2.1	Precursors used for sample preparations. . . . .	37
3.1	Various structural parameters, and agreement factors obtained from the Rietveld (LRO) and PDF (SRO) refinements of the X-ray diffraction patterns and PDF profile for $x = 0.40$ <i>via</i> monoclinic ( $Pm$ ) model at LRO and SRO respectively. . . . .	63

3.2	Various structural parameters, and agreement factors obtained from the Rietveld (LRO) and PDF (SRO) refinements of the X-ray diffraction patterns and PDF profile for $x = 0.50$ via monoclinic ( $Pm$ ) model at LRO and SRO respectively. . . . .	63
3.3	Various structural parameters, and agreement factors obtained from the Rietveld (LRO) and PDF (SRO) refinements of the X-ray diffraction patterns and PDF profile for $x = 0.60$ via monoclinic ( $Pm$ ) model at LRO and SRO respectively. . . . .	65
3.4	Frozen phonon modes for low symmetry distorted structure ( $Pm$ ). . . . .	75
3.5	Amplitude of the phonon mode(s) in low symmetry ferroelectric phase (monoclinic, $Pm$ ) of $KNN_x$ (0.40, 0.50, and 0.60) ceramics, with respect to high symmetry cubic ( $Pm\bar{3}m$ ) phase. . . . .	76
4.1	Various structural phase transitions in $KBST_x$ ceramics. . . . .	86
4.2	Various structural parameters, and agreement factors obtained from the Rietveld refinements of the X-ray diffraction patterns (at ambient conditions) for $x = 0.00$ ( $KNN_{50}$ ) using the $Pm$ model. . . . .	87
4.3	Various structural parameters, and agreement factors obtained from the Rietveld refinements of the X-ray diffraction patterns (at ambient conditions) for $x = 0.05$ ( $KBST_5$ ) using ( $Pm + P4mm$ ) model. . . . .	87
4.4	Various structural parameters, and agreement factors obtained from the Rietveld refinements of the X-ray diffraction patterns (at ambient conditions) for $x = 0.10$ ( $KBST_{10}$ ) using ( $Pm + P4mm$ ) model. . . . .	87
4.5	Various structural parameters, and agreement factors obtained from the Rietveld refinements of the X-ray diffraction patterns (at ambient conditions) for $x = 0.15$ ( $KBST_{15}$ ) using $P4mm$ model. . . . .	88

4.6	Various temperatures corresponding to the real part of the dielectric constant of $\text{KBST}_x$ ceramics. Here, $T_C$ is the Curie temperature for normal ferroelectrics (for $0.00 \leq x \leq 0.15$ ), and $T_m$ is the temperature corresponding to dielectric maxima observed for ceramics exhibiting diffuse phase transitions ( $x = 0.20$ ). Note: The temperatures corresponding to KNN50 ceramics have been taken from the literature (Kong <i>et al.</i> , 2021). . . . .	88
4.7	Description of various irreps corresponding to the cubic and monoclinic phase with $Pm\bar{3}m$ , $P4mm$ , and $Pm$ space groups, respectively. . . . .	97
5.1	CTE values for different oxide perovskite materials where $\alpha_l$ and $\alpha_v$ represent linear and volumetric CTE. . . . .	115
6.1	Various structural parameters and agreement factors obtained from the Rietveld refinements of the X-ray diffraction patterns (at ambient conditions) for $x = 1.00$ via tetragonal ( $P4mm$ ) model. . . . .	130
6.2	Various structural parameters and agreement factors obtained from the Rietveld refinements of the X-ray diffraction patterns (at ambient conditions) for $x = 0.95$ via cubic ( $Pm\bar{3}m$ ) model. . . . .	130
6.3	Various structural parameters and agreement factors obtained from the Rietveld refinements of the X-ray diffraction patterns (at ambient conditions) for $x = 0.90$ via cubic ( $Pm\bar{3}m$ ) model. . . . .	131
6.4	Description of various Raman modes observed in temperature-dependent Raman spectra of $\text{KBST}_{90}$ ceramics, where "s" and "as" in the subscript represent symmetric and asymmetric nature of modes, respectively. . . . .	138
6.5	Various structural parameters obtained for $\text{KBST}_{90}$ ceramics from the PDF refinements at 100 K for different length scales. . . . .	142
6.6	Various structural parameters obtained for $\text{KBST}_{90}$ ceramics from the PDF refinements at 300 K for different length scales. . . . .	142

6.7	Various structural parameters obtained for KBST90 ceramics from the PDF refinements at 500 K for different length scales. . . . .	142
7.1	Debye temperature ( $\theta_D$ ), volume at 0 K ( $V_0$ ), SVFS ( $\omega_S$ ), and volumetric coefficient of thermal expansion (CTE; $\alpha_V$ ) for the phases at long/short ranges. . . . .	160